An Accurate Dead Time Compensation Method for SPWM Voltage Source Inverters

Jie Ye, Yukai Huang, Songtao Huang, *Graduate Student Member, IEEE*,
Haozhe Wang, *Student Member, IEEE*, Baojin Li, Jinbang Xu, and Anwen Shen, *Member, IEEE*

***Abstract*—Dead time is generally used to avoid the short circuit of the dc source, which causes harmonics in the output voltage and current of the voltage source inverters (VSIs). Based on an accurate harmonics calculation model of digital sinusoidal pulsewidth modulation, harmonics caused by dead time can be analyzed and calculated accurately. The proposed method obtains the compensation waveforms by the derived calculation module and detailed operation steps and then injects these into the sinusoidal reference voltage to eliminate the corresponding frequency harmonics caused by the dead time effect. The phase delay of the fundamental voltage caused by dead time is also considered. Moreover, this method avoids detecting the current polarity, affecting the compensation effect. Simulation and experimental results of the proposed method are presented to validate the effectiveness.**

***Index Terms*—Dead time compensation, digital sinusoidal pulsewidth modulation, harmonics, voltage source inverter (VSI).**

I. INTRODUCTION

THE pulsewidth modulation (PWM) voltage source inverter is one of the most commonly used topology structures in power electronics and has important applications in new energy power generation, motor control, and power supply fields [1], [2], [3]. Generally, to prevent a short circuit of the dc bus in an inverter leg, the dead time is added in PWM signals. However, the added dead time will result in the distortion of the output voltage and current, which is called the dead time effect.

To compensate the dead time effect, many methods have been proposed. There are the following three main compensation methods based on the analysis of generation of the dead time effect.

1) *Average value theory*: In most instances, the compensation techniques based on the average value theory are used to eliminate the dead time effect [4], [5], [6], [7], [8]. Seung-Gi and Min-Ho [4] modified the reference wave to compensate the output voltage. These methods depended on the polarity of the current, which was the key to the compensation strategy. Hence, other methods have been proposed to improve the compensation effect and solve the current detection problems. Munoz and Lipo [5] used an instantaneous back calculation of the phase angle of the current to obtain the zero crossing of the current. For three-phase systems, the compensation voltage can be obtained by a startup measurement in the stationary reference frames [6]. Similarly, Zhao et al. [7] used the average value theory to minimize the $6n$th harmonics of the current in the synchronously rotating reference frame to obtain the exact compensation voltage. Li et al. [8] reconstructed the pulse sequence so that the current over zero position can be predicted and then used the average value theory for harmonic compensation to reduce the error caused by the current over zero detection.
2) Pulse-based compensation methods [9], [10], [11], [12]: Murai et al. [9] used a correction circuit to change the pulse width to compensate for the pulse of the previous moment. The pulse-based dead time compensator was proposed in [10], which will adjust each PWM pulse to correct the voltage distortion. Such schemes cannot modify the pulse width effectively if the modulation index is relatively reaching the maximum or the minimum pulse width. To deal with this situation, the authors in [11] and [12] adjusted the switching frequency and PWM according to the operating conditions, which require additional hardware and lots of effort to determine the stable parameter set.
3) Dead time elimination [13], [14], [15], [16]: The authors in [13] and [14] decomposed the generic phase-leg into two basic switching cells, which are configured with a controllable switch in series with an uncontrollable diode, hence, the dead time is not needed. However, the additional detection circuit to detect the current direction of the antiparallel is sensitive to the current ripple and will also increase the number of fault points. Song et al. [15] used a tri-carrier phase-shift sinusoidal pulsewidth modulation (SPWM) modulation method and some logic operations to eliminate the dead time effect, which is complicated to implement. Yan et al. [16] used a double modulated waveform for the dead time effect to be eliminated.

In addition to these methods, many software-based solutions have also been put forward. The authors in [17], [18], and [19] are

---

Manuscript received 9 August 2022; revised 30 October 2022; accepted 30 November 2022. Date of publication 5 December 2022; date of current version 14 February 2023. This work was supported by the Natural Science Foundation of China under Grant 62173156. Recommended for publication by Associate Editor D. C. Lee. *(Corresponding author: Yukai Huang.)*

The authors are with the National Key Laboratory of Science and Technology on Multispectral Information Processing and Key Laboratory of Image Processing and Intelligent Control, School of Artificial Intelligence and Automation, Huazhong University of Science and Technology, Wuhan 430074, China (e-mail: yejie_hust@hust.edu.cn; hyk_aia@hust.edu.cn; songtao_huang@hust.edu.cn; wanghaozhe@hust.edu.cn; lbj_jiayou@hust.edu.cn; xujinbang@mail.hust.edu.cn; sawyi@mail.hust.edu.cn).

Color versions of one or more figures in this article are available at https://doi.org/10.1109/TPEL.2022.3226865.

Digital Object Identifier 10.1109/TPEL.2022.3226865

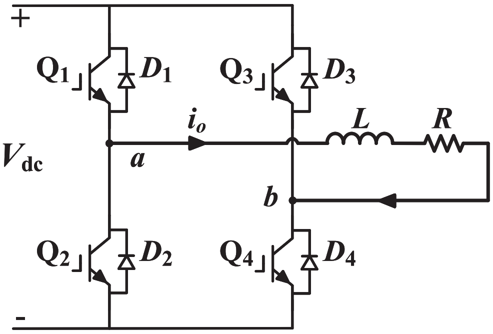

Fig. 1. Single-phase VSI structure diagram.

based on disturbance observer to obtain the dead time compensation voltage, which require precise parameters of the inverter model and motor model. The authors in [20] and [21] adopt self-tuning methods to compensate the voltage distortion caused by the nonlinearity of inverters. Although it is possible to obtain better results with these methods, lots of experience and effort are required to acquire adequate values of the tunable parameters.

In this article, an accurate harmonic calculation model for the unipolar SPWM is established to accurately analyze the dead time effect and obtains an expression of the harmonic calculation. A dead time compensation method is proposed based on harmonic injection. The proposed method can compensate the low-frequency harmonics caused by the dead time effect. Simulations and experiments verify the modulation model and compensation method. Experimental results show that the compensation method is feasible and effective.

The main contributions of this article are as follows.

1) A more accurate calculation model for unipolar SPWM modulation is derived. This harmonic calculation model is closer to the actual modulation model.
2) Detecting the current polarity is not needed, so the performance of the proposed compensation method would not be affected by the current ripple and zero current clamping.
3) The solution equations of the proposed compensation method are simplified by the Taylor expansion, which are simple to implement in the control chip.

The rest of this article is organized as follows. Section II analyzes the dead time effect in unipolar SPWM, and the expression of the harmonic calculation is derived. Section III presents the compensation method to compensate the dead time effect. They are verified by simulations and experiments in Sections IV. Finally, Section V concludes this article.

II. DEAD TIME EFFECT AND CALCULATION MODEL

A. Dead Time Effect

Fig. 1 shows the topology of the signal-phase VSI. In Fig. 1, Q_1–Q_4 and D_1–D_4 are power switches and antiparallel diodes. V_{dc} denotes the dc-bus voltage. V_o and i_o are the output voltage and current of the VSI, respectively.

Fig. 2 shows the output voltage distortion caused by the dead time effect. During the dead time, switches in the same phase-leg are turned OFF. Due to the i_o currents through the inductor that cannot be changed instantaneously, it flows through the corresponding antiparallel diodes, which causes the voltage distortion.

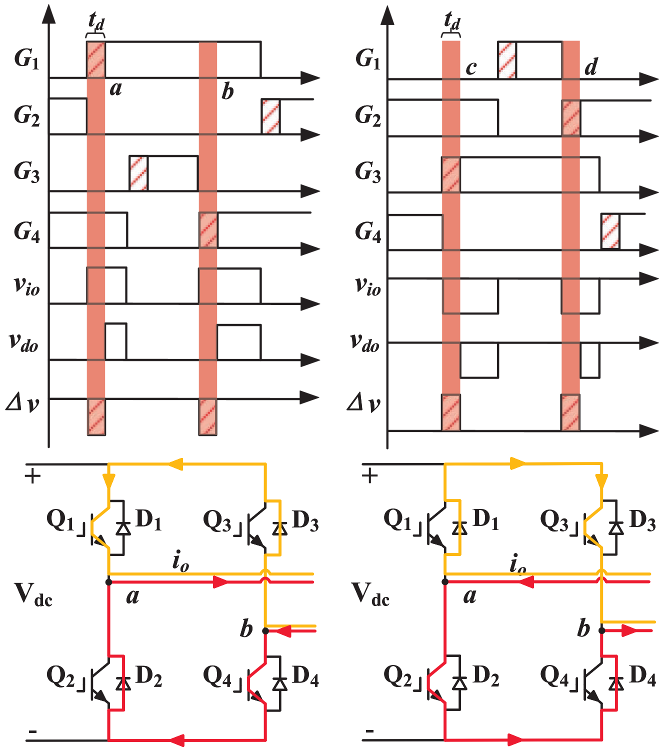

(a) (b)

Fig. 2. Influence of the dead time effect on the output voltage. (a) $i_o > 0$. (b) $i_o < 0$.

In Fig. 2, v_{io} and v_{do} are the ideal output voltage and the actual output voltage, respectively. G_1–G_4 are actual drive signals of switches with dead time t_d. As shown at point a in Fig. 2(a), Q_1 and Q_2 are both turned OFF when G_1 is delayed by dead time t_d. Then, if the output current i_o is greater than zero, it flows through D_2 and Q_4. Similarly, when G_4 is also delayed, Q_3 and Q_4 are turned OFF, as shown at point b. The current i_o flows through Q_1 and D_3. In the abovementioned two cases, v_{do} will be different from v_{io} when the output current i_o is greater than zero. The error between v_{do} and v_{io} is defined as Δv and can be expressed as

$$\Delta v = v_{\mathrm{do}} - v_{io}. \tag{1}$$

On the other hand, when the output current i_g is less than zero, the Δv is analyzed in the same way as shown in Fig. 2(b).

B. Dead Time Calculation Model Analysis

One of the most common modulation strategies for the VSI is the unipolar SPWM, or known as the three-level PWM, which requires two modulated waveforms u_m and $-u_m$. The dead time effect with the unipolar SPWM is shown in Fig. 3. The digital controller is widely used in inverter systems, which can only process digital signals. To be closer to the actual system, the

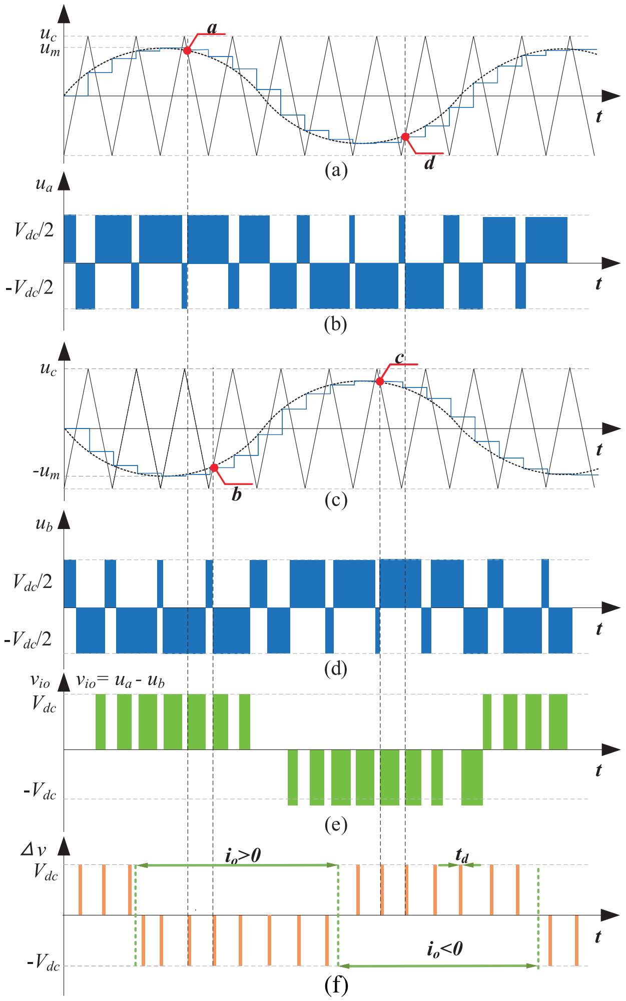

Fig. 3. (a)–(f) Schematic diagram of the digital unipolar SPWM modulation and the dead time effect.

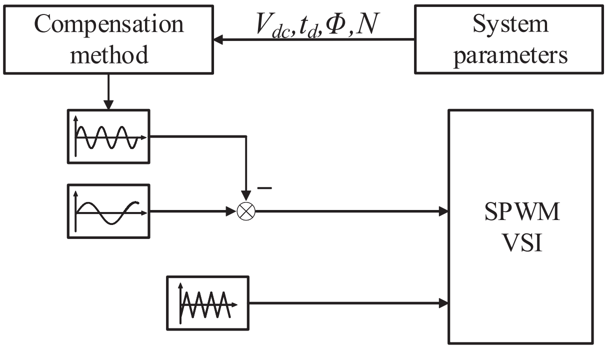

Fig. 4. Block diagram with the proposed dead time compensation method.

modulated waveform is digitized. Fig. 3(a)–(e) shows the output voltage generation of the unipolar SPWM. It uses one common carrier waveform u_c and two π-shifted sinusoidal reference waveforms, u_m and $-u_m$. u_m is used to generate the voltage of the left phase-leg u_a and $-u_m$ is used to generate the voltage of the right phase-leg u_b. The output voltage of the VSI is the subtraction of u_a and u_b, as shown in Fig. 3(e). Fig. 3(f) shows the distribution of error voltage analyzed in Fig. 2. For the harmonic analysis model of actual output voltage v_{do}, it can be divided into two parts according to (1): the ideal output voltage v_{io} as shown in Fig. 3(e) and the error voltage Δv caused by the dead time effect, as shown in Fig. 3(f).

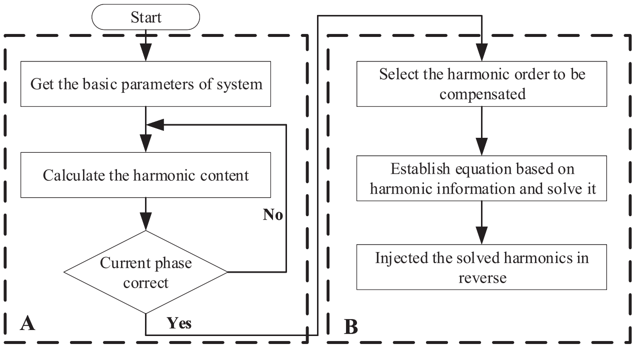

Fig. 5. Flowchart of the compensation method.

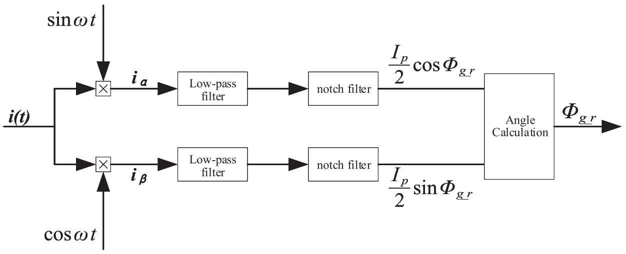

Fig. 6. Current decomposition into phase angle.

The most well-known analysis method of determining the harmonic components of an ideal PWM-switch inverter was first developed by Bowes and Bird [22]. However, the analysis of dead time is not performed. Ye et al. [23] proposed a harmonic calculation for digital bipolar modulation considering dead time, which approximates the actual system closely, and optimized in [24]. However, as a widely used modulation strategy, the unipolar SPWM is not performed in the calculation model. Combining the analysis methods in [22] and [23], the error voltage Δv of unipolar SPWM can be accurately derived by double fourier integral analysis (DFIA) as

$$\begin{aligned}\Delta v = {} & \frac{1}{2}A_{00} + \sum_{n=1}^{\infty}\left(A_{0n}\cos ny + B_{0n}\sin ny\right) \\ & + \sum_{m=1}^{\infty}\left(A_{m0}\cos mx + B_{m0}\sin mx\right) \\ & + \sum_{m=1}^{\infty}\sum_{n=\pm1\ldots}^{\pm\infty}\left\{\begin{array}{l}A_{mn}\cos\left(mx+ny\right) \\ +B_{mn}\sin\left(mx+ny\right)\end{array}\right\}\end{aligned} \tag{2}$$

where $x = \omega_c t$, $y = \omega_m t$, ω_c, and ω_m are the triangular carrier angular frequency and the modulation wave angular frequency. A_{mn} and B_{mn} denote the DFIA coefficients and are defined as

$$A_{mn} + jB_{mn} = \frac{1}{2\pi^2}\int_{-\pi}^{\pi}\int_{-\pi}^{\pi}\Delta v e^{j(mx+ny)}dxdy. \tag{3}$$

Fig. 3(f) shows that the pulses of error voltage Δv consist of two parts. One part produced by the modulated waveform u_m is Δu_{mp}, and the other part produced by the modulated waveform $-u_m$ is Δu_{np}, hence, Δv can also be expressed as

$$\Delta v = \Delta u_{mp} + \Delta u_{mn}. \tag{4}$$

The mathematical expression of the error voltage Δv can be obtained by deriving the DFIA expressions of Δu_{mp} and Δu_{mn}, respectively. According to Figs. 2 and 3, the error voltage Δu_{mp} can be defined as

$$\Delta u_{mp} = \begin{Bmatrix} E & x_{p1} < x < x_{p1} + t_d, i_o < 0 \\ -E & x_{p2} < x < x_{p2} + t_d, i_o > 0 \end{Bmatrix} \tag{5}$$

where x_{p1} and x_{p2} are the switching instants of the error voltage, E is the dc voltage V_{dc}. They are given as [23]. Substituting (5) into (3), the DFIA coefficient of Δu_{mn} can be expressed as follows:

$$\begin{aligned} &Ap_{mn} + jBp_{mn} \\ &= \frac{1}{2\pi^2} \int_{-\pi+\varphi}^{\varphi} \int_{\frac{\pi}{2}(1+M\sin y_f)}^{\frac{\pi}{2}(1+M\sin y)+\omega_c t_d} E e^{j\left(mx+n\left(y+\frac{x}{N}\right)\right)} dx dy \\ &\quad \frac{1}{2\pi^2} \int_{\varphi}^{\pi+\varphi} \int_{-\frac{\pi}{2}(1+M\sin y)}^{-\frac{\pi}{2}(1+M\sin y)+\omega_c t_d} -E e^{j\left(mx+n\left(y+\frac{x+\pi}{N}\right)\right)} dx dy \end{aligned} \tag{6}$$

where φ is the phase angle of the current and $N = \omega_c/\omega_m$ is defined as the carrier ratio. The inner integration in (6) can be further derived to (7) shown at the bottom of this page. It should be mentioned that (7) cannot be simplified into a simple cumulative form because the integral limit $(-\pi + \varphi, \varphi)$ and $(\varphi, \pi + \varphi)$ are not symmetrical, such as $(-\pi, \pi)$. As for Δu_{mn}, its DFIA coefficient is shown as (8) shown at the bottom of this page, and the derivation process is similar to (7) except that the switching instants are changed. Combining (7) and (8), the DFIA coefficient of error voltage Δv can be represented as (9) shown at the bottom of this page.

The mathematical expression of the ideal voltage v_{io} can also be obtained through a similar derivation process of the error voltage Δv. However, the difference is that v_{io} can be simplified to simple cumulative form as shown in (10) shown at the bottom of this page, depending on the Bessel function integral relationships in Appendix A. Finally, combining the DFIA coefficients of v_{io} and Δv, the DFIA of actual output voltage v_{do} is shown in (11). Where θ_1 is the phase angle of the sinusoidal reference waveform. This expression can calculate the harmonic content through the current phase, which will play an important role in the proposed compensation method. It should also be noted that E denotes the average of the dc voltage, so when the value E is used for the calculation, the ripples of the dc voltage do not have a large impact on the calculation of (11) shown at the bottom of this page:

$$Ae_{mp} + jBe_{mp} = \frac{E}{2j\left(m+\frac{n}{N}\right)\pi^2} \left(e^{j\left(m+\frac{n}{N}\right)\omega_c t_d} - 1\right) e^{j\frac{n}{2N}\pi} \begin{Bmatrix} e^{j\frac{\pi}{2}m} \int_{-\pi+\varphi}^{\varphi} e^{j\frac{\pi}{2}\left(m+\frac{n}{N}\right)M\sin y_r} e^{jny_r} dy_r \\ -e^{-j\frac{\pi}{2}m} \int_{\varphi}^{\pi+\varphi} e^{-j\frac{\pi}{2}\left(m+\frac{n}{N}\right)M\sin y_f} e^{jny_f} dy_f \end{Bmatrix} \tag{7}$$

$$Ae_{mn} + jBe_{mn} = \frac{E}{2j\left(m+\frac{n}{N}\right)\pi^2} \left(e^{j\left(m+\frac{n}{N}\right)\omega_c t_d} - 1\right) e^{j\frac{n}{2N}\pi} \begin{Bmatrix} e^{-j\frac{\pi}{2}m} \int_{-\pi+\varphi}^{\varphi} e^{j\frac{\pi}{2}\left(m+\frac{n}{N}\right)M\sin y_r} e^{jny_r} dy_r \\ -e^{j\frac{\pi}{2}m} \int_{\varphi}^{\pi+\varphi} e^{-j\frac{\pi}{2}\left(m+\frac{n}{N}\right)M\sin y_f} e^{jny_f} dy_f \end{Bmatrix} \tag{8}$$

$$A_{\Delta v\_mn} + jB_{\Delta v\_mn} = \frac{E}{j\left(m+\frac{n}{N}\right)\pi^2} \left(e^{j\left(m+\frac{n}{N}\right)\omega_c t_d} - 1\right) e^{j\frac{n}{2N}\pi} \cos\frac{\pi}{2}m \begin{Bmatrix} \int_{-\pi+\varphi}^{\varphi} e^{j\frac{\pi}{2}\left(m+\frac{n}{N}\right)M\sin y_r} e^{jny_r} dy_r \\ -\int_{\varphi}^{\pi+\varphi} e^{-j\frac{\pi}{2}\left(m+\frac{n}{N}\right)M\sin y_f} e^{jny_f} dy_f \end{Bmatrix} \tag{9}$$

$$\begin{aligned} u_{ab} = &\sum_{n=1,3,5\ldots}^{\infty} \begin{Bmatrix} -\frac{4EN}{n\pi} J_n\left[\frac{nM\pi}{2N}\right] \sin\left(\frac{n\pi}{2N} - n\theta_1\right) \cos\left(ny + n\theta_1\right) \\ +\frac{4EN}{n\pi} J_n\left[\frac{nM\pi}{2N}\right] \cos\left(\frac{n\pi}{2N} - n\theta_1\right) \sin\left(ny + n\theta_1\right) \end{Bmatrix} \\ &+ \sum_{m=2,4\ldots}^{\infty} \sum_{n=\pm1,\pm3\ldots}^{\pm\infty} \begin{Bmatrix} -\frac{4E}{\left(m+\frac{n}{N}\right)\pi} J_n\left[\left(m+\frac{n}{N}\right)\frac{M\pi}{2}\right] \sin\left(\frac{n\pi}{2N} - n\theta_1\right) \cos\frac{m}{2}\pi \cos\left(mx + ny + mN\theta_1 + n\theta_1\right) \\ +\frac{4E}{\left(m+\frac{n}{N}\right)\pi} J_n\left[\left(m+\frac{n}{N}\right)\frac{M\pi}{2}\right] \cos\left(\frac{n\pi}{2N} - n\theta_1\right) \cos\frac{m}{2}\pi \sin\left(mx + ny + mN\theta_1 + n\theta_1\right) \end{Bmatrix} \end{aligned} \tag{10}$$

$$\begin{aligned} v_{\text{do}} = &\sum_{n=1,3,5\ldots}^{\infty} \begin{Bmatrix} -\frac{4EN}{n\pi} J_n\left[\frac{nM\pi}{2N}\right] \sin\left(\frac{n\pi}{2N} - n\theta_1\right) \cos\left(ny + n\theta_1\right) + A_{\Delta v\_0n} \\ +\frac{4EN}{n\pi} J_n\left[\frac{nM\pi}{2N}\right] \cos\left(\frac{n\pi}{2N} - n\theta_1\right) \sin\left(ny + n\theta_1\right) + B_{\Delta v\_0n} \end{Bmatrix} \\ &+ \sum_{m=2,4\ldots}^{\infty} \sum_{n=\pm1,\pm3\ldots}^{\pm\infty} \begin{Bmatrix} -\frac{4E}{\left(m+\frac{n}{N}\right)\pi} J_n\left[\left(m+\frac{n}{N}\right)\frac{M\pi}{2}\right] \sin\left(\frac{n\pi}{2N} - n\theta_1\right) \cos\frac{m}{2}\pi \cos\left(mx + ny + mN\theta_1 + n\theta_1\right) \\ +\frac{4E}{\left(m+\frac{n}{N}\right)\pi} J_n\left[\left(m+\frac{n}{N}\right)\frac{M\pi}{2}\right] \cos\left(\frac{n\pi}{2N} - n\theta_1\right) \cos\frac{m}{2}\pi \sin\left(mx + ny + mN\theta_1 + n\theta_1\right) \end{Bmatrix} \\ &+ \sum_{m=1,2,3}^{\infty} \sum_{n=\pm1,\pm2,\pm3}^{\pm\infty} \left\{A_{\Delta v\_mn} \cos\left(mx + ny\right) + B_{\Delta v\_mn} \sin\left(mx + ny\right)\right\}. \end{aligned} \tag{11}$$

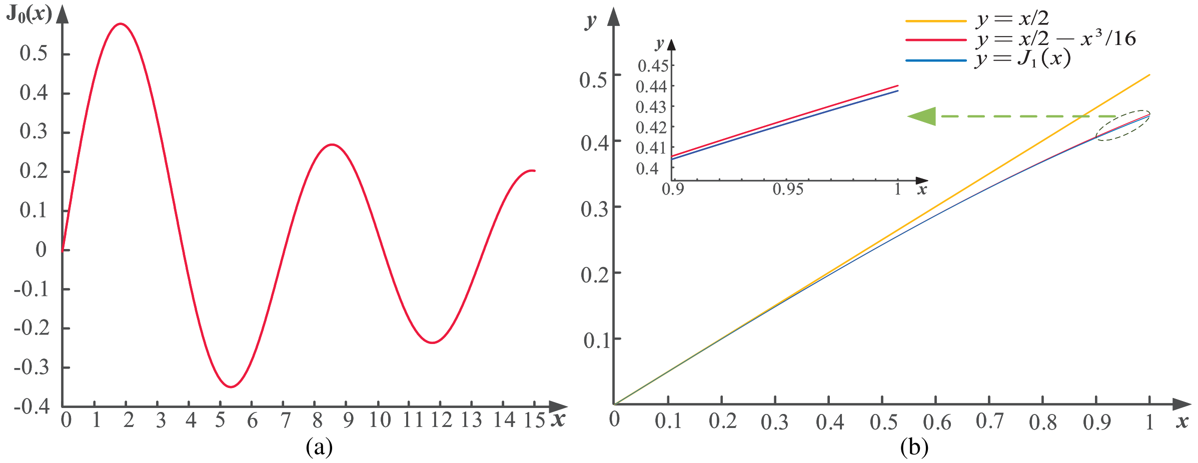

Fig. 7. (a) Function curve of first-order Bessel function. (b) Comparison of the function curves among first-order Taylor expansion, second-order Taylor expansion and first-order Bessel function.

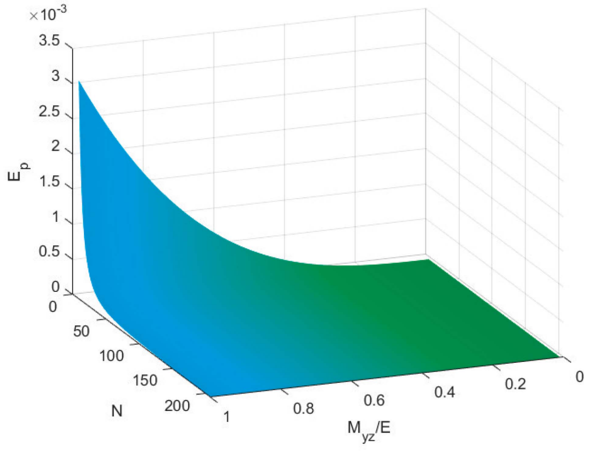

Fig. 8. Surface of the error.

III. PROPOSED DEAD TIME COMPENSATION METHOD

The dead time effect results in output voltage distortion, which is mainly reflected in the increase in low-frequency harmonics. For this reason, a compensation method based on harmonic injection is proposed in this section. The scheme is depicted in Fig. 4. First, get the basic parameters of the system. The required parameters for the harmonics calculation are the dc-bus voltage V_{dc}, the dead time t_d, the modulation frequency f_m, the carrier frequency f_c, the carrier ratio N, and the phase angle of current Φ. Next, various orders of harmonics are generated by the compensation method to compensate the dead time effect. The flowchart of the compensation method is shown in Fig. 5 and it can be divided into the following two parts: harmonic information acquisition and the establishment and solution of equations.

A. Harmonic Information Acquisition

It can be observed from Fig. 4 that the acquisition of harmonic information is the first and essential step of the compensation strategy. As shown in Fig. 5, the first step is to obtain the basic parameters of the system to calculate the harmonic content. The mathematical model of the actual output voltage established in Section II can calculate the harmonic accurately. Therefore, the second step in Fig. 5 is to calculate the harmonic content according to (11) and the calculated values of the model can be the estimated values of the actual harmonic.

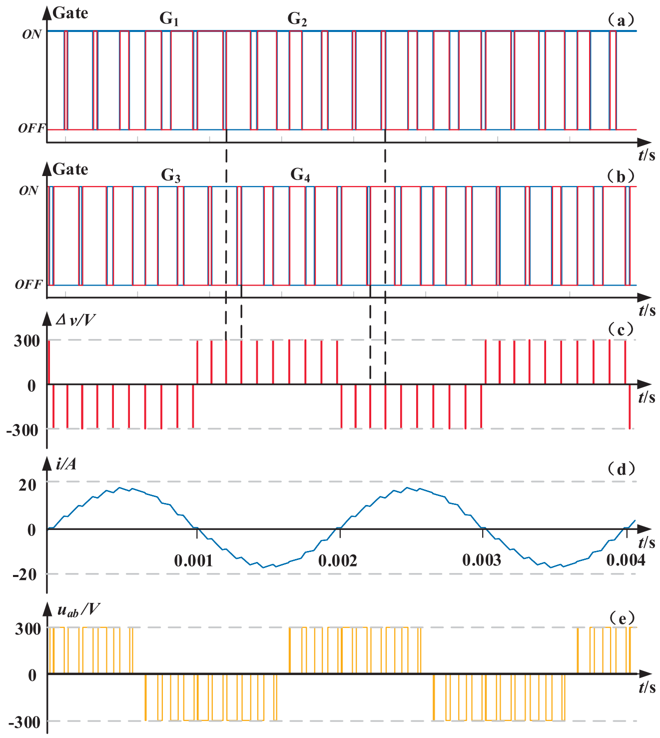

Fig. 9. Unipolar SPWM simulation of VSI at f_m=500 Hz, f_c=5 kHz.

However, when the dead time is added to the actual inverter operation, the output voltage is distorted, and the phase angle of the fundamental voltage is delayed, resulting in a deviation in the current phase calculation. Hence, a secondary calculation method is adopted to obtain the accurate phase angle of the

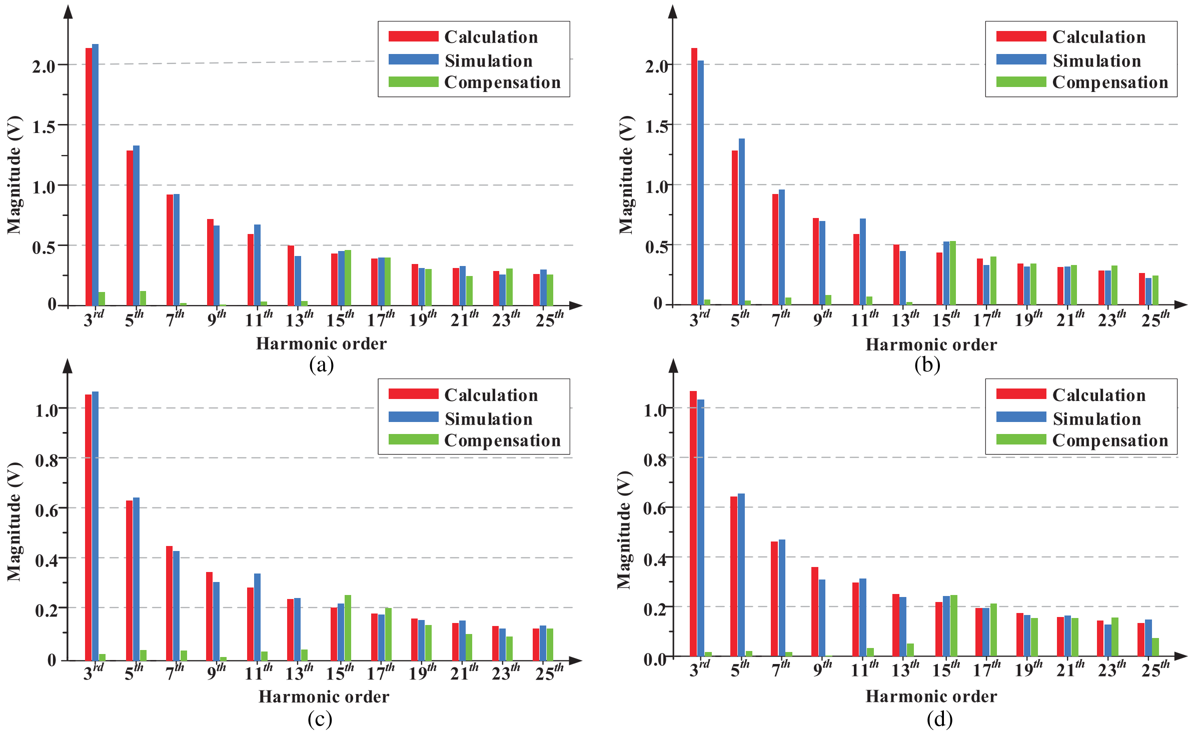

Fig. 10. Comparison of voltage harmonics with different dead times and modulation indexes at $f_c = 10$ kHz and $f_m = 50$ Hz. (a) $M = 0.8$, $t_d = 1$ us. (b) $M = 0.2$, $t_d = 1$ us. (c) $M = 0.8$, $t_d = 0.5$ us. (d) $M = 0.2$, $t_d = 0.5$ us.

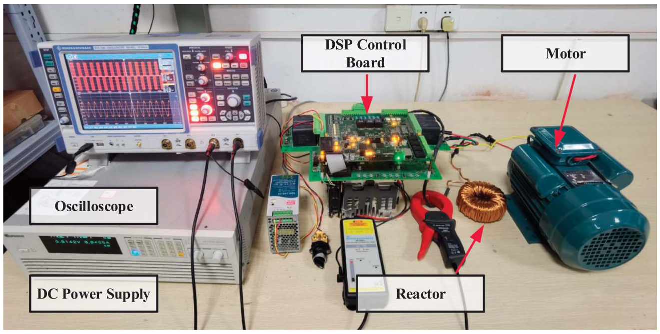

Fig. 11. Experimental platform.

output current by considering the influence of the dead time effect on the fundamental voltage, which is the third step of the flowchart.

The current phase correction is as follows. If the load impedance is known, the current I_{g_r} without considering the dead time effect can be obtained by (12)

$$I_{g\_r} = \frac{U_m}{Z_g} \tag{12}$$

where U_m and Z_g are the reference voltage and the load impedance, respectively. Φ_{g_r} is the phase angle of the current I_{g_r}. Next, through the ideal current phase angle Φ_{g_r}, the output voltage with dead time effect can be calculated by (11) to obtain the fundamental voltage phase delay $\Delta\Phi$ for the first time. And then the estimated value of the actual phase angle of the current Φ_g can be expressed as

$$\Phi_g = \Phi_{g\_r} + \Delta\Phi. \tag{13}$$

Finally, the harmonic components of the output voltage need to be recalculated with the corrected phase angle Φ_g. The above is the first part of the compensation method, as shown in Fig. 5. In practical situations, the load impedance is not easy to know well, hence, a coordinate system transformation can be used to obtain the load power factor in [5]

$$\begin{aligned} i_\alpha &= I_{\text{peak}} \sin(\omega t + \Phi_{g\_r}) \sin(\omega t) \\ &= \frac{I_{\text{peak}}}{2} \left(\cos(\Phi_{g\_r}) - \cos(2\omega t + \Phi_{g\_r})\right) \end{aligned} \tag{14}$$

and

$$\begin{aligned} i_\beta &= I_{\text{peak}} \sin(\omega t + \Phi_{g\_r}) \cos(\omega t) \\ &= \frac{I_{\text{peak}}}{2} \left(\sin(2\omega t + \Phi_{g\_r}) + \sin(\Phi_{g\_r})\right) \end{aligned} \tag{15}$$

where I_{peak} is the peak value of the current. Φ_{g_r} can be obtained with the low-pass filter and second-order notch filter, as shown in Fig. 6. The low-pass filter is used to eliminate the high-frequency components introduced by the PWM frequency. The notch-type filter, tuned at twice the excitation frequency, is used to eliminate the double-frequency terms in (14) and (15). It should also be noted that the phase angle can also be obtained by other methods.

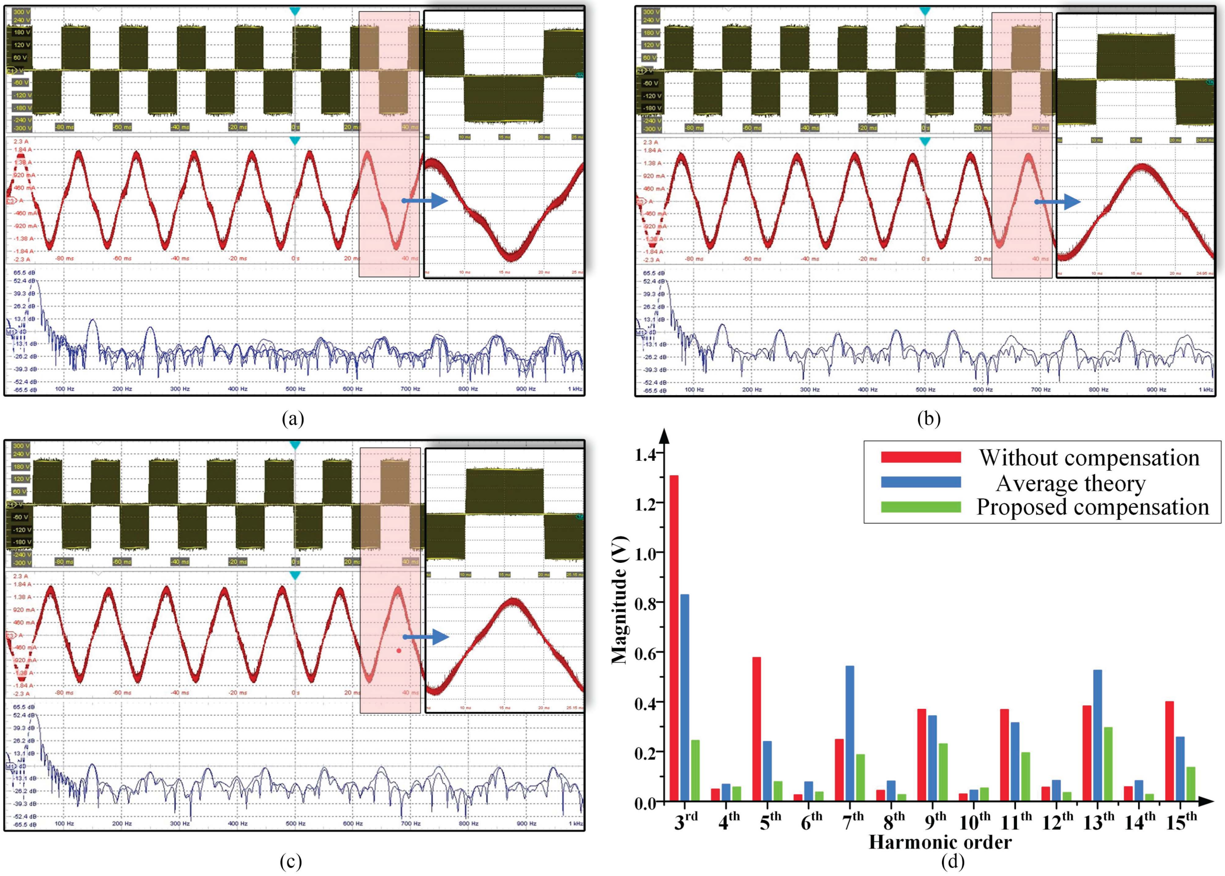

(a) (b) (c) (d)

Fig. 12. Comparison of output voltages, stator currents, and FFT analysis of output voltage under 50 Hz, t_{d1} and modulation index 0.8. (a) Without compensation method. (b) Average theory compensation. (c) Proposed compensation method. (d) Comparison of output voltage harmonics magnitude under different methods.

B. Establishment and Solution of Equations

After obtaining the harmonic information, which harmonics to choose to compensate and how to obtain the compensated harmonic information are the next points to consider. As shown in Fig. 5, the fourth step is to select the harmonic order to be compensated after obtaining the harmonic content. The third to 15th odd harmonics are selected to compensate in this article since the content of odd harmonics is large in low-frequency band. Of course, higher frequency harmonics can also be compensated. However, in the low-frequency band, the higher the harmonic order, the smaller the content. Moreover, the high-frequency harmonics can be eliminated by designing a suitable filter [25], which is not the focus of this article. The last step establishes an equation based on harmonic information and solves it in order to obtain the modulation ratio and phase of the injected compensation waveforms. The final injected harmonic voltage can be described as

$$V_i = \sum_{n=3}^{+\infty} V_{\mathrm{dc}} p \sin\left(n\omega_m t + \theta_n\right) \tag{16}$$

where n is the selected order of injected harmonic and ω_m is the fundamental angular frequency. p and θ_n are modulation index and phase angle of the injected harmonic, respectively. Obviously, p and θ_n need to be solved for the injected harmonics. How to establish equations for solving p and θ_n is the key to the compensation method.

According to the derivation process in Section II, it is observed that the position of the intersection of the modulated waveform and the high-frequency carrier waveform affects the distribution of the error wave and further determines the harmonic phase. Compared with the original modulated waveform, the magnitude of the injected harmonic is smaller, which means that the modulated waveform will not be greatly changed after injection. Therefore, it is assumed that the harmonic content generated by the original modulated waveform will not be affected after the compensation waveforms are injected. Then, the fundamental wave generated by the injected harmonic is able to eliminate the harmonic of the same frequency. If the abovementioned assumptions are satisfied, the equations can be established as

$$\begin{cases} \left(A_{01}\right)^2 + \left(B_{01}\right)^2 = M_{yz}^2 & (a) \\ \arctan\left(\frac{A_{01}}{B_{01}}\right) = \varPhi_{yz} & (b) \end{cases} \tag{17a}$$

$$A_{01} = -\frac{4EN}{\pi} J_1\left[\frac{p\pi}{2N}\right] \sin\left(\frac{\pi}{2N} - \theta_n\right)$$

$$B_{01} = \frac{4EN}{\pi} J_1\left[\frac{p\pi}{2N}\right] \cos\left(\frac{\pi}{2N} - \theta_n\right) \tag{17b}$$

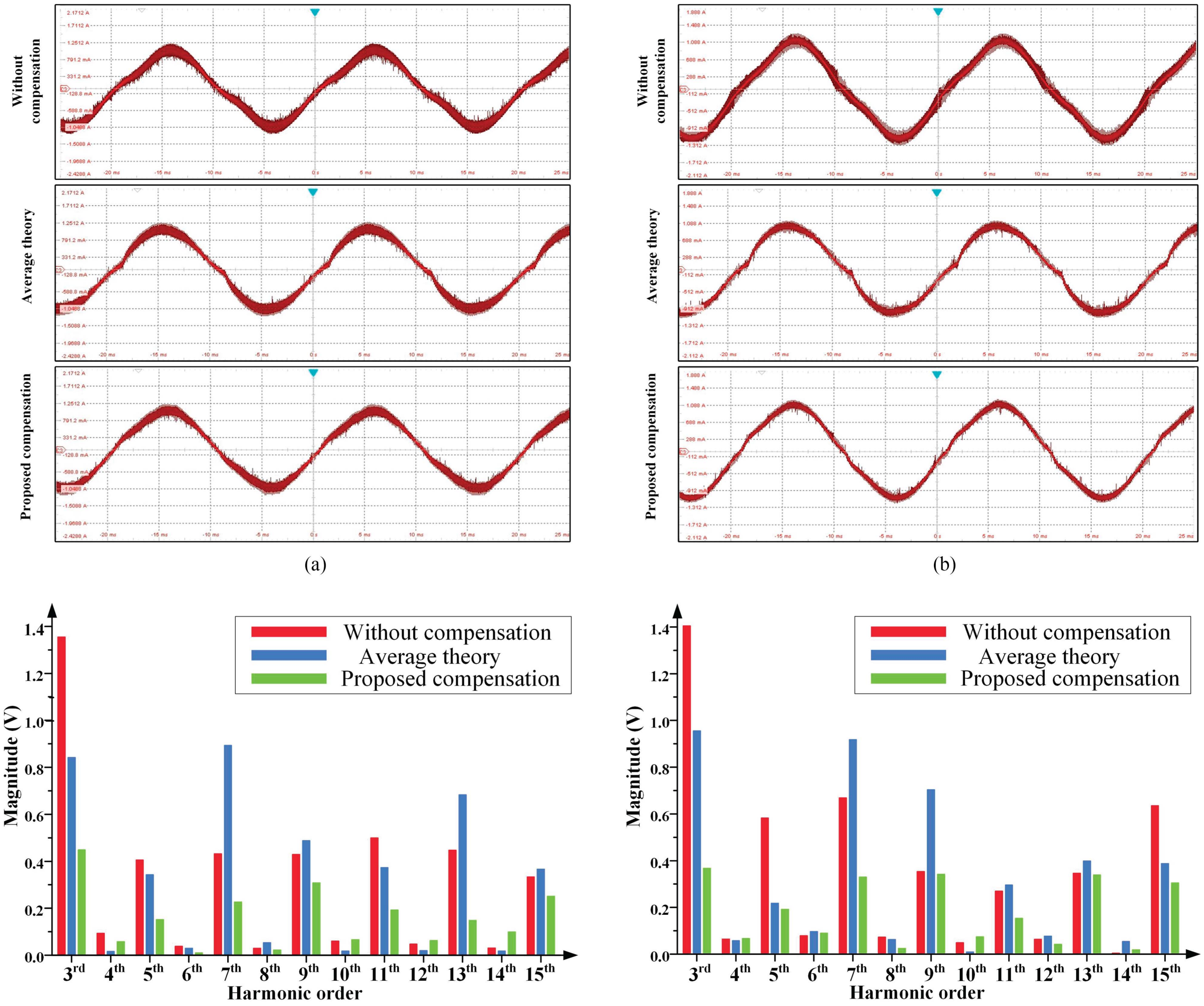

(a) (b) (c) (d)

Fig. 13. Comparison of the stator currents and FFT analysis of output voltages under 50 Hz, t_{d1} and different modulation indexes. (a) Comparison of the stator currents at a modulation index of 0.4. (b) Comparison of the stator currents at a modulation index of 0.2. (c) FFT results at a modulation index of 0.4. (d) FFT results at a modulation index of 0.2.

$$\left\{\begin{array}{ll} \frac{4EN}{\pi} J_1\left[\frac{p\pi}{2N}\right] = M_{yz} & (a) \\ \theta_n = \Phi_{yz} + \frac{\pi}{2N} & (b) \end{array}\right\} \tag{17c}$$

where p and θ_n are the target variables to be solved. M_{yz} and Φ_{yz} are the known magnitude and phase angle of harmonic obtained from the previous analysis.

The left-hand side of (17a), A_{01} and B_{01} are the fundamental component expression of the injected waveform, which can be obtained from (10) when $n = 1$ and $m = 0$, as shown in (17b). Substituting (17b) into (17a) to obtain the simplified equations (17c), which can show the relationship between the solved variables and the known variables.

The abovementioned analysis shows that (11) is more accurate than (10) due to considering the dead time effect, but it is unsuitable as the left-hand side of (17a). There are two parts in (11). One part is the ideal modulation harmonics and the other part is the harmonics generated by the dead time effect. If (11) is used as the left-hand side of (17a), which means that the fundamental component of the injected waveforms and the harmonics generated by the dead time effect are equal to the harmonics that need to be compensated. In fact, the harmonics generated by the dead time effect result from the interaction of the injection waveform and modulation waveform, which cannot be calculated by the injection waveform alone. Moreover, it has been assumed that the injection waveform has little effect on the harmonics generated by the dead time effect. Consequently, the fundamental component generated by the injected waveform can be taken as the left-hand side of (17a) and it can be simplified to (17c). As shown in Fig. 5, the compensation waveform can be obtained by (17c), and then injected into the original modulated waveform in reverse.

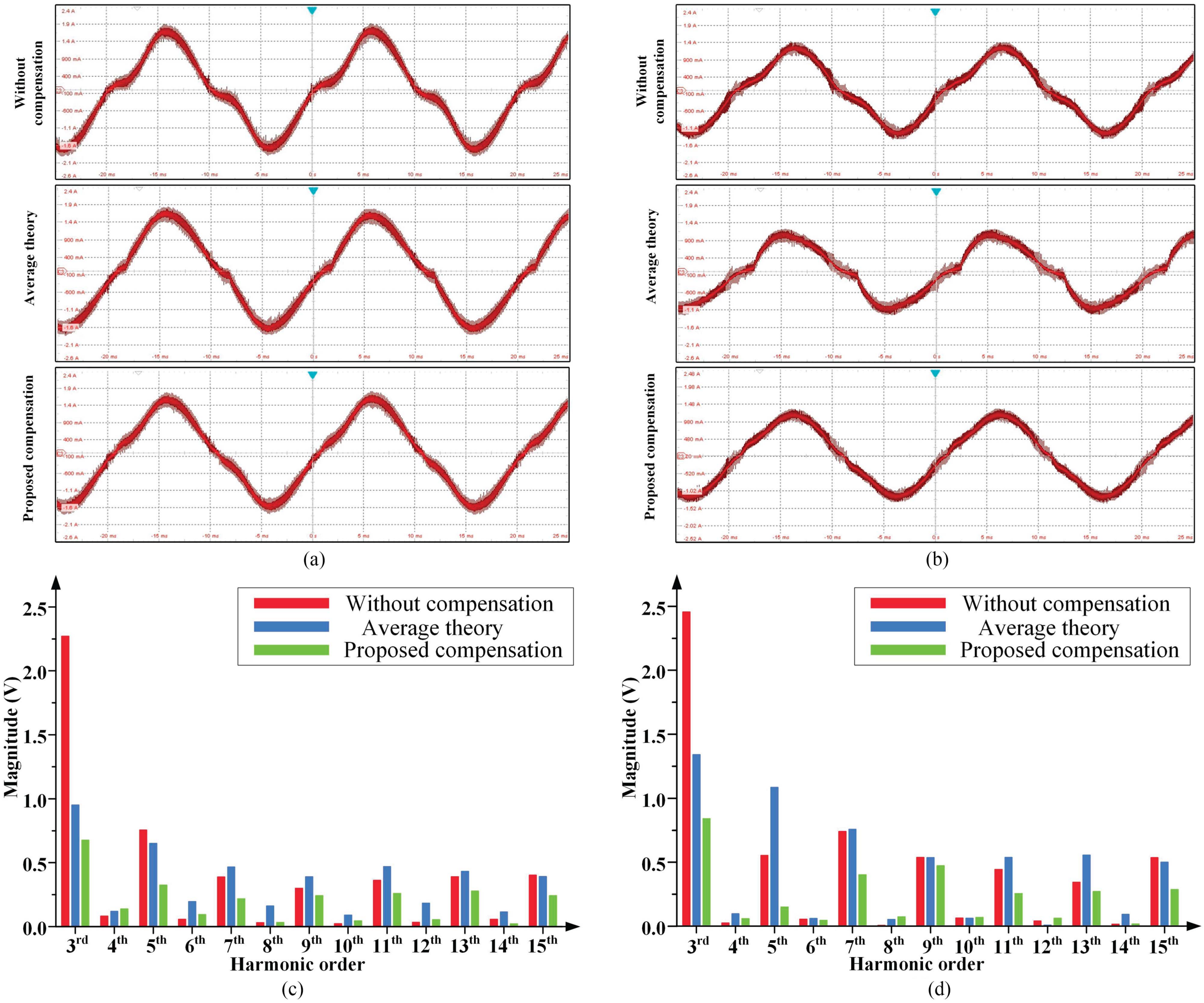

(a) (b) (c) (d)

Fig. 14. Comparison of the stator currents and FFT analysis of output voltages under 50 Hz, t_{d2} and different modulation indexes. (a) Comparison of the stator currents at a modulation index of 0.8. (b) Comparison of the stator currents at a modulation index of 0.2. (c) FFT results at a modulation index of 0.8. (d) FFT results at a modulation index of 0.2.

However, solving (17c) is difficult due to the Bessel function in a nonlinear equation. Further analysis of the equation is required to obtain the p and θ_n. $\frac{p\pi}{2N}$ in (17c) is in (0,1) for $p \in (0,1)$ and $N \gg 1$. The first-order Bessel function curve is shown in Fig. 7(a). It can be observed that the function monotonically increases if $x \in (0,1)$. The second-order Taylor expansion of the Bessel function can be obtained as follows in Appendix B

$$\begin{aligned} J_1(x) &= \sum_{m=0}^{\infty} \frac{(-1)^m}{m!\Gamma(m+2)} \left(\frac{x}{2}\right)^{2m+1} \\ &\approx \frac{1}{\Gamma(2)} \frac{x}{2} + \frac{-1}{\Gamma(3)} \frac{x^3}{8} \\ &\approx \frac{x}{2} - \frac{x^3}{16}. \end{aligned} \tag{18}$$

The comparison of the function curves among the first-order Taylor expansion, second-order Taylor expansion, and first-order Bessel function is shown in Fig. 7(b). It can be seen that the second-order Taylor expansion is very close to the original function on the interval [0,1], while the first-order Taylor expansion is close to the other two functions near the origin. Generally, the carrier wave ratio N is greater than or equal to 10, hence, $\frac{p\pi}{2N} \leq 0.157$ and (17c) can be simplified with the first-order Taylor expansion as follows:

$$\begin{aligned} \frac{4EN}{\pi}\left(\frac{1}{2} \cdot \frac{p\pi}{2N}\right) &\approx M_{yz} \\ p &\approx \frac{M_{yz}}{E} \end{aligned} \tag{19a}$$

and

$$\begin{Bmatrix} p \approx \frac{M_{yz}}{E} & (a) \\ \theta_n = \Phi_{yz} + \frac{\pi}{2N} (b) \end{Bmatrix}. \tag{19b}$$

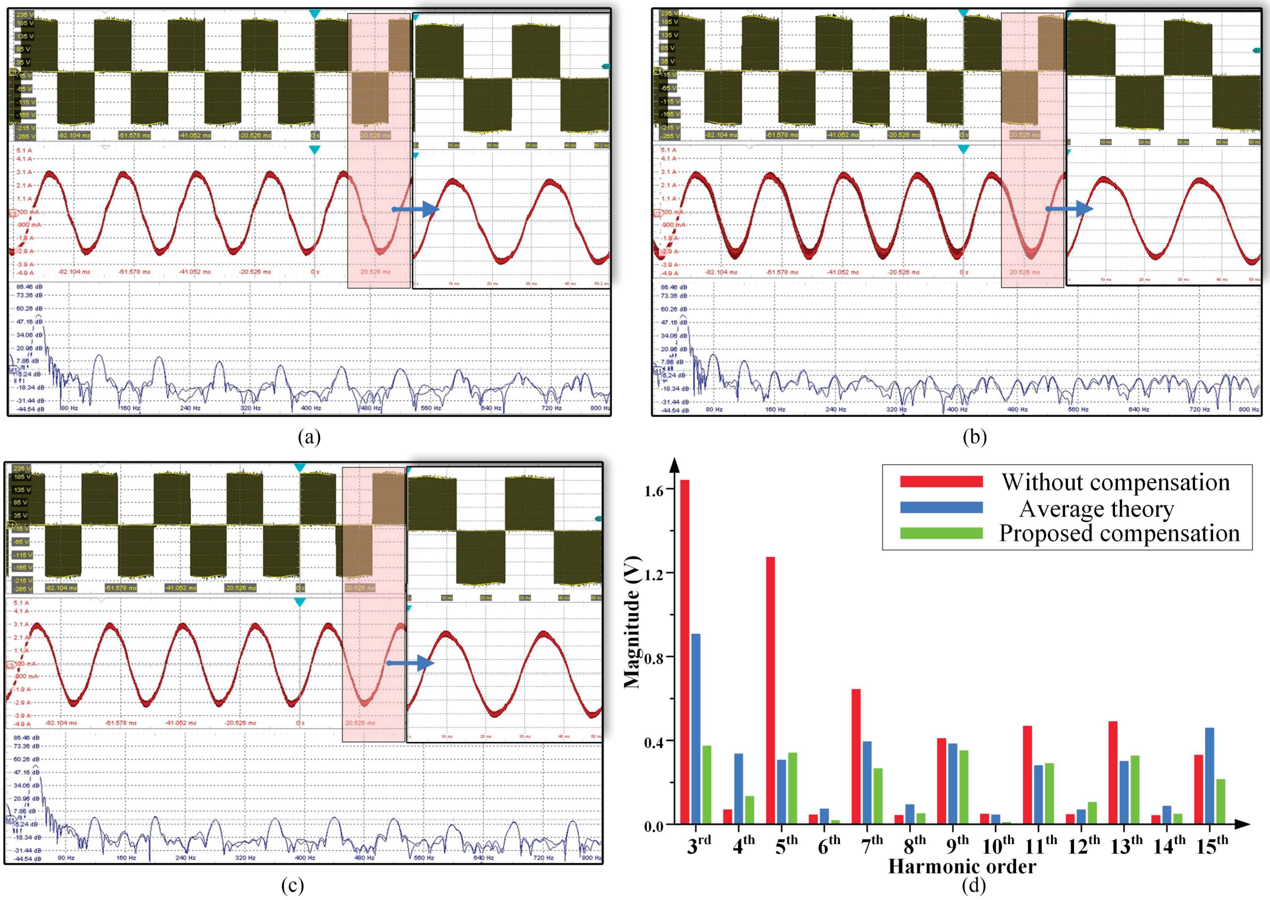

(a) (b) (c) (d)

Fig. 15. Comparison of output voltages, stator currents and FFT analysis of output voltage under 40Hz, t_{d1} and modulation index 0.8. (a) without compensation. (b) With the average theory compensation. (c) With the proposed dead time compensation. (d) Comparison of output voltage harmonics magnitude under different methods.

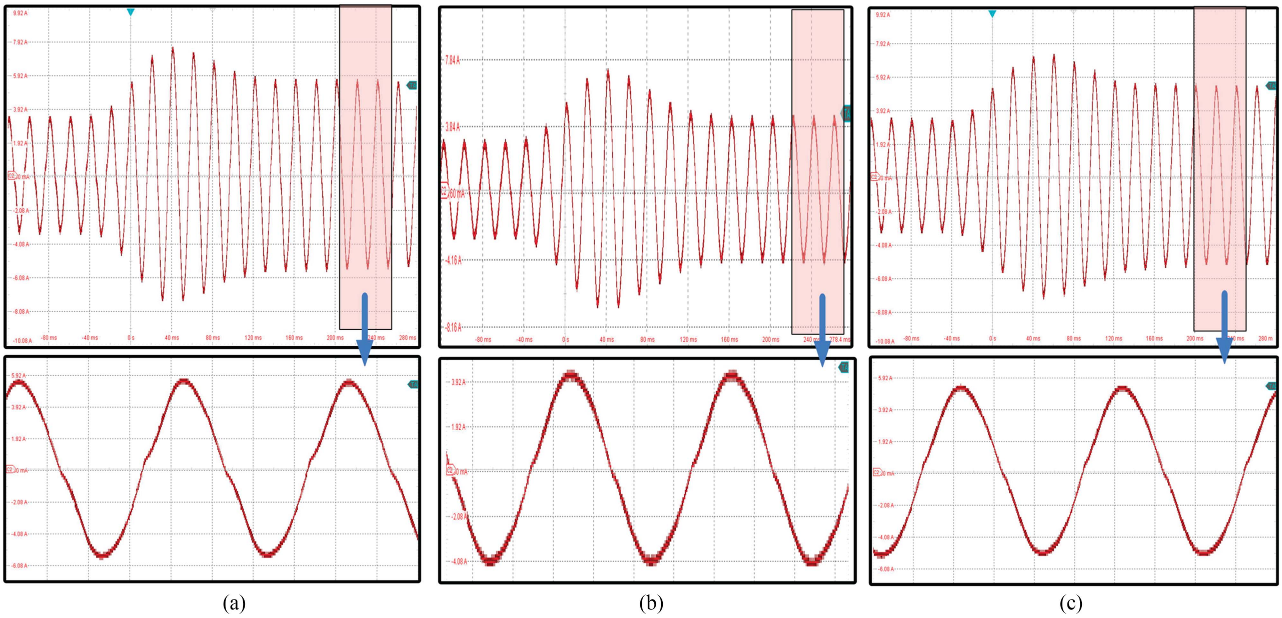

(a) (b) (c)

Fig. 16. Stator current waveforms under the transient state. (a) Without the dead time compensation. (b) With the average theory compensation. (c) With the proposed dead time compensation.

From (19b), it is shown that p and θ_n can be obtained by solving linear equations, which can reduce calculation resources and the solving difficulty. The final compensation waveforms are injected into the original modulation waveform, which is the final step of the compensation method, as shown in Fig. 5.

C. Error Analysis

In order to solve (17c), the first-order Taylor expansion of the Bessel function is utilized to simplify the equation and the error should be analyzed. In Fig. 7(b), it can be seen that the second-order Taylor expansion is very close to the original Bessel function on the interval [0,1]. Substituting (18) into (17c) gives the following more accurate equation:

$$\left(\frac{p\pi}{2N}\right)^3 - 8\cdot\left(\frac{p\pi}{2N}\right) + 16\left(\frac{M_{yz}\pi}{4EN}\right) = 0$$

$$x_s^3 - 8x_s + 16A = 0 \tag{20}$$

where $x_s = \frac{p\pi}{2N}$, $A = \frac{M_{yz}\pi}{4EN}$ and (20) can be solved with the Appendix C (the formula of extracting roots on cubic equation)

$$p_s = x_s \cdot \frac{2N}{\pi}$$

$$p_s = \begin{pmatrix} \omega\sqrt[3]{-\frac{16A}{2} + \sqrt{\left(\frac{16A}{2}\right)^2 + \left(\frac{-8}{3}\right)^3}} \\ +\omega^2\sqrt[3]{-\frac{16A}{2} - \sqrt{\left(\frac{16A}{2}\right)^2 + \left(\frac{-8}{3}\right)^3}} \end{pmatrix} \frac{2N}{\pi}. \tag{21}$$

Therefore, the error E_p of using an approximation of the modulation index can be expressed as

$$\begin{aligned} E_p &= p_s - p \\ &= \begin{pmatrix} \omega\sqrt[3]{-\frac{16A}{2} + \sqrt{\left(\frac{16A}{2}\right)^2 + \left(\frac{-8}{3}\right)^3}} \\ +\omega^2\sqrt[3]{-\frac{16A}{2} - \sqrt{\left(\frac{16A}{2}\right)^2 + \left(\frac{-8}{3}\right)^3}} \end{pmatrix} \frac{2N}{\pi} - \frac{M_{yz}}{E} \\ &= \begin{pmatrix} \omega\sqrt[3]{-\frac{2\pi}{N}\cdot\frac{M_{yz}}{E} + \sqrt{\left(\frac{2\pi}{N}\cdot\frac{M_{yz}}{E}\right)^2 + \left(\frac{-8}{3}\right)^3}} \\ +\omega^2\sqrt[3]{-\frac{2\pi}{N}\cdot\frac{M_{yz}}{E} - \sqrt{\left(\frac{2\pi}{N}\cdot\frac{M_{yz}}{E}\right)^2 + \left(\frac{-8}{3}\right)^3}} \end{pmatrix} \frac{2N}{\pi} \\ &\quad - \frac{M_{yz}}{E} \end{aligned} \tag{22}$$

where p_s and p are solutions of equations using second-order Taylor expansion and first-order Taylor expansion, respectively. It can be seen that E_p is a function of two variables N and M_{yz}/E. Since M_{yz} is the magnitude of the output voltage, M_{yz}/E is in (0,1). N is the carrier wave ratio, which can be within [10,200]. The error function surface is presented in Fig. 8. As can be seen, the error E_p increases as M_{yz}/E increases and N decreases. The maximum error is less than 0.0035. However, for the M_{yz}/E, the ratio of the harmonic amplitude and the dc voltage is much less than 1 in practical situations, which means that the error will be very small. Therefore, the error approximated using the modulation ratio is small.

TABLE I
PARAMETERS OF THE SIMULATION SYSTEM

Symbol	Parameters	Value
V_{dc}	DC-bus voltage	250 V
f_m	Modulation frequency	50/100/500 Hz
f_c	Carrier frequency	5/10 kHz
L	Reactor inductance	0.8 mH
R_L	Resistance	0.75 Ω
Δt	Dead time	0.5 μs/1 μs

IV. SIMULATION AND EXPERIMENTAL RESULTS

A. Simulink and Result Analysis

The MATLAB/Simulink model of a single-phase VSI is built to verify the time domain model and compensation strategy. The simulation parameters are shown in Table I. In order to verify the effectiveness of the compensation strategy, the simulations are performed under different modulation indexes and dead times.

Fig. 9 shows the main waveforms of the unipolar SPWM simulation of VSI. In order to display the error waveform more clearly, a smaller carrier ratio is selected. Fig. 7(a) and (b) shows the gating signals of the power switches Q_1–Q_4. Fig. 9(c) and (d) shows the error voltage and output current, respectively. Fig. 9(e) shows the actual output voltage with dead time. The gating signals are generated by the unipolar SPWM, as shown in Fig. 3 As shown in Fig. 9, the corresponding relationship between the error waveform's position and the gating signals' position is consistent with the analysis in Section II.

Fig. 10 shows the magnitude comparison of output voltage harmonics among the simulation without compensation, simulation with compensation and the calculation. Fig. 10(a)–(d) shows the results with different dead times and modulation indexes at $f_c = 10$ kHz and $f_m = 50$ Hz. As shown in Fig. 10, the calculation result in (11) is consistent with the simulation without compensation, which can prove the accuracy of the calculation model for the unipolar SPWM derived in Section II. The third- to 13th-order harmonics are compensated with the proposed method. Fig. 10(a) and (b) shows the performance of the proposed compensation method at the high modulation index ($M = 0.8$) and the low modulation index ($M = 0.2$), respectively. The dead time is configured at 1 μs. It can be seen that the magnitude of these compensated harmonics decrease greatly. Fig. 10(c) and (d) shows the performance of the compensation method with a shorter dead time of 0.5 μs. It can be observed that the harmonic content is also greatly reduced as the dead time is reduced and the proposed method still has a good harmonic suppression performance.

Table II shows the comparison results between the proposed method and the average theory method. The proposed method has a similar or even better performance for the compensated harmonics than the average theory method. Indeed, the average theory method has a suppressive effect on all low-frequency harmonics caused by dead time. In order to eliminate more harmonics, more order compensation waveforms need to be injected. However, for the high-order harmonic, the

TABLE II
COMPARISON RESULTS OF DIFFERENT COMPENSATION METHODS

Modulation index	Dead time	Carrier frequency	Compensation method	Third	Fifth	Seventh	Ninth	11^{th}	13^{th}
0.1	1 μs	10 kHz	Without compensation	2.2	1.22	0.92	0.76	0.57	0.45
			Proposed method	0.19	0.18	0.06	0.08	0.1	0.06
			Average theory method	0.36	0.47	0.38	0.44	0.38	0.37
0.2	1 μs	10 kHz	Without compensation	2.03	1.38	0.96	0.69	0.71	0.44
			Proposed method	0.04	0.03	0.06	0.08	0.07	0.03
			Average theory method	0.08	0.15	0.07	0.15	0.07	0.10
0.4	1 μs	10 kHz	Without compensation	2.09	1.34	0.98	0.63	0.74	0.47
			Proposed method	0.06	0.09	0.07	0.03	0.05	0.09
			Average theory method	0.12	0.16	0.08	0.12	0.06	0.11
0.8	1 μs	10 kHz	Without compensation	2.17	1.32	0.92	0.66	0.67	0.41
			Proposed method	0.03	0.09	0.08	0.09	0.05	0.08
			Average theory method	0.1	0.16	0.13	0.12	0.07	0.12
1	1 μs	10 kHz	Without compensation	2.15	1.32	0.98	0.69	0.62	0.39
			Proposed method	0.09	0.02	0.03	0.06	0.05	0.08
			Average theory method	0.42	0.21	0.28	0.1	0.01	0.16

TABLE III
EXPERIMENTAL SYSTEM PARAMETERS

Symbol	**Parameters**	**Value**
V_{dc}	DC-bus voltage	200 V
S_r	Motor rated power	2.2 kW
V_r	Motor rated voltage	220 V
F_r	Motor rated frequency	50 Hz
f_m	Modulation frequency	50/40 Hz
f_c	Carrier frequency	10 kHz
L_1	Reactor inductance	4 mH
R_{L1}	Internal resistance of reactor	0.14 Ω
t_{d1}	Dead time	1 μs
t_{d2}	Dead time	2 μs

frequency is higher, which can be filtered out by designing a suitable filter. Thus, there is no need to inject too high-order harmonics.

B. Experimental Results

The proposed compensation method has been implemented in the experimental platform, as shown in Fig. 11. The core of the control system is TI's DSP(TMS320F28377D). The dc-bus voltage is generated by a programmable dc power supply (Chroma 62150H-600S). The compensation method is implemented with different dead times and modulation indexes. The parameters of the system are shown in Table III.

The magnitude and phase angles of the third to 15th injected waveforms under different conditions are obtained with the proposed compensation method and shown in Table IV. Through the steps shown in Fig. 5 and the linear equations (19b), compensating waveforms of corresponding order can be calculated and injected by the lookup table.

Fig. 12 shows the comparison of the output voltages, the stator currents, and fast Fourier transform (FFT) analysis of the output voltage when the motor is running at 50 Hz with t_{d1} and modulation index 0.8 (mechanically 1200 r/min). It can be observed from Fig. 12(a) that the current has obvious distortion in the zero-crossing area and the voltage has low-frequency harmonics due to the dead time effect. Fig. 12(b) shows the compensation effect of the average theory method. The current waveform is still slightly distorted in the zero-crossing area since the average theory compensation method requires current zero-crossing detection, which may cause a control delay and misjudgment of the current polarity. The low-frequency harmonics are also not well suppressed. Comparing the results in Fig. 12(a) and (b), the proposed method improves the current distortion caused by dead time, as shown in Fig. 12(c). The third to 15th harmonics are compensated in this example. As can be seen from the FFT analysis waveforms, the corresponding harmonics are closer to 0 Bb in Fig. 12(c) than in (a) and (b). Fig. 12(d) shows the comparison of the harmonic contents more clearly.

Fig. 13(a) and (c) shows the comparison of the stator currents and the FFT analysis of the output voltage when the modulation index is 0.4. Fig. 13(b) and (d) shows the same comparison except that the modulation index is 0.2. It can be clearly observed that the current waveform of the proposed compensation is more sinusoidal compared to the current waveform of the uncompensated one, while the average theory compensation method is sensitive to the influence of the current zero-crossing and the compensation effect is reduced. Figs. 12(d), 13(c) and (d) show the results of the low-frequency harmonics compensation at different modulation indexes. The proposed compensation method is confirmed to perform well with a wider range of modulation indexes.

Fig. 14 shows similar comparison results to Fig. 13, with the difference that the dead time is t_{d2} and the modulation ratios are 0.8 and 0.2, respectively. It can be seen that the low-frequency harmonics increase and the current is severely distorted as the dead time increases. The proposed compensation method

TABLE IV
CALCULATION RESULTS OF INJECTED HARMONICS

Modulation index	Dead time	Compensation content	Third	Fifth	Seventh	Ninth	11^{th}	13^{th}	15^{th}
0.8	t_{d1}	Magnitude	0.00513	0.00308	0.00221	0.00172	0.00142	0.00120	0.00103
		Phase angle	132.26	100.13	68.21	36.39	4.57	–27.83	–59.08
0.8	t_{d2}	Magnitude	0.0103	0.00617	0.00441	0.00344	0.00283	0.00239	0.00209
		Phase angle	134.99	104.58	74.52	44.49	14.22	–15.91	–45.69

TABLE V
COMPARISON OF STATOR CURRENT HARMONICS

Compensation method	THD	Third	Fifth	Seventh	Ninth
Without Compensation	6.87%	0.641	0.385	0.151	0.087
Average theory method	4.67%	0.427	0.254	0.085	0.066
Proposed method	4.70%	0.319	0.224	0.083	0.063

can also have an excellent suppressive effect on low-frequency harmonics caused by dead time.

Fig. 15 compares the output voltage among no compensation, the average theory compensation, and the proposed method's compensation with the motor running at 40 Hz, t_{d1}, and the modulation index of 0.8. It can be seen that the current waveform is optimized by the proposed method compared to the case without compensation, and the effect of the average theory compensation is similar. Then, comparing the specific amplitude of each harmonic, as shown in Fig. 15(d), it can be seen that the effect of the proposed method on harmonic compensation is better than the average theory compensation.

Fig. 16 shows the stator current waveforms during the transient. In the results, the proposed method well compensates the dead time effect at the transient as well as the steady state. The overshoot at the transient is due to the mechanical response of the load, and when the load is stabilized, it can be seen that the compensated stator current waveform is more sinusoidal than the uncompensated one. For a better comparison with the average theory method, the specific amplitudes of each harmonic of the current and THD are compared in Table V. It can be seen that both the average theory method and the proposed method can compensate well the harmonics and reduce the THD. Comparing each harmonic's amplitude, it can be found that the proposed method is better than the average theory method for the third and fifth harmonics. The seventh and ninth harmonics are similarly compensated to small amplitudes. The THD of the average method is slightly smaller than that of the proposed method because the averaging method is based on the average-value theory to compensate for the full-band harmonics generated by the dead time, while the proposed method compensates for specific harmonics. The frequency band of harmonic compensation can be increased for different needs.

V. CONCLUSION

In this article, a dead time compensation method is proposed based on accurate harmonic injection. Considering the voltage hysteresis with dead time, a secondary calculation method is adopted for harmonic acquisition. Moreover, Taylor expansion transforms nonlinear equations into linear equations, which can reduce calculation resources and the difficulty of solving. The proposed method does not require additional hardware to detect the current polarity. The low-frequency harmonics of the output voltage can be well compensated and the output current becomes more sinusoidal. Simulation and experimental results verify the effectiveness of the proposed compensation method. However, the proposed method still has some limitations when the load changes frequently. Future work will focus on simplifying the process in this case.

APPENDIX A
BESSEL FUNCTION INTEGRAL RELATIONSHIPS

$$e^{\pm j\xi\cos\theta} = J_0(\xi) + 2\sum_{k=1}^{+\infty} j^{\pm k} J_k(\xi)\cos(k\theta) \tag{23}$$

$$\int_{-\pi}^{\pi} e^{\pm j\xi\cos\theta}\cos(n\theta)d\theta = 2\pi j^{\pm n} J_n(\xi) \tag{24}$$

$$\int_{-\pi}^{\pi} e^{\pm j\xi\cos\theta}\sin(n\theta)d\theta = 0. \tag{25}$$

APPENDIX B
SERIES FORMULA OF BESSEL FUNCTION BESSEL FUNCTION

$$J_\alpha(x) = \sum_{m=0}^{\infty} \frac{(-1)^m}{m!\Gamma(m+\alpha+1)}\left(\frac{x}{2}\right)^{2m+\alpha}. \tag{26}$$

APPENDIX C
FORMULA OF EXTRACTING ROOTS ON CUBIC EQUATION

$$\begin{aligned}
&x^3 + px + q = 0\\
&x_1 = \sqrt[3]{-\frac{q}{2} + \sqrt{\left(\frac{q}{2}\right)^2 + \left(\frac{p}{3}\right)^3}}\\
&\quad + \sqrt[3]{-\frac{q}{2} - \sqrt{\left(\frac{q}{2}\right)^2 + \left(\frac{p}{3}\right)^3}}\\
&x_2 = \omega\sqrt[3]{-\frac{q}{2} + \sqrt{\left(\frac{q}{2}\right)^2 + \left(\frac{p}{3}\right)^3}}\\
&\quad + \omega^2\sqrt[3]{-\frac{q}{2} - \sqrt{\left(\frac{q}{2}\right)^2 + \left(\frac{p}{3}\right)^3}}
\end{aligned}$$

$$\begin{aligned} x_3 &= \omega^2 \sqrt[3]{-\frac{q}{2} + \sqrt{\left(\frac{q}{2}\right)^2 + \left(\frac{p}{3}\right)^3}} \\ &\quad + \omega \sqrt[3]{-\frac{q}{2} - \sqrt{\left(\frac{q}{2}\right)^2 + \left(\frac{p}{3}\right)^3}} \\ \omega &= \frac{-1 + i\sqrt{3}}{2}. \end{aligned} \tag{27}$$

REFERENCES

[1] J. I. Leon, S. Kouro, L. G. Franquelo, J. Rodriguez, and B. Wu, "The essential role and the continuous evolution of modulation techniques for voltage-source inverters in the past, present, and future power electronics," *IEEE Trans. Ind. Electron.*, vol. 63, no. 5, pp. 2688–2701, May 2016.

[2] X. Liang, "Emerging power quality challenges due to integration of renewable energy sources," *IEEE Trans. Ind. Appl.*, vol. 53, no. 2, pp. 855–866, Mar./Apr. 2017.

[3] G. Feng, C. Lai, W. Li, Z. Li, and N. C. Kar, "Dual reference frame based current harmonic minimization for dual three-phase PMSM considering inverter voltage limit," *IEEE Trans. Power Electron.*, vol. 36, no. 7, pp. 8055–8066, Jul. 2021.

[4] S.-G. Jeong and M.-H. Park, "The analysis and compensation of dead-time effects in PWM inverters," *IEEE Trans. Ind. Electron.*, vol. 38, no. 2, pp. 108–114, Apr. 1991.

[5] A. Munoz and T. Lipo, "On-line dead-time compensation technique for open-loop PWM-VSI drives," *IEEE Trans. Power Electron.*, vol. 14, no. 4, pp. 683–689, Jul. 1999.

[6] J.-W. Choi and S.-K. Sul, "Inverter output voltage synthesis using novel dead time compensation," *IEEE Trans. Power Electron.*, vol. 11, no. 2, pp. 221–227, Mar. 1996.

[7] H. Zhao, Q. Wu, and A. Kawamura, "An accurate approach of nonlinearity compensation for VSI inverter output voltage," *IEEE Trans. Power Electron.*, vol. 19, no. 4, pp. 1029–1035, Jul. 2004.

[8] B. Li et al., "A new model-based dead time compensation strategy for cascaded H-Bridge converters," *IEEE Trans. Ind. Electron.*, to be published, doi: 10.1109/TIE.2022.3177757.

[9] Y. Murai, T. Watanabe, and H. Iwasaki, "Waveform distortion and correction circuit for PWM inverters with switching lag-times," *IEEE Trans. Ind. Appl.*, vol. IA-23, no. 5, pp. 881–886, Sep. 1987.

[10] D. Leggate and R. Kerkman, "Pulse-based dead-time compensator for PWM voltage inverters," *IEEE Trans. Ind. Electron.*, vol. 44, no. 2, pp. 191–197, Apr. 1997.

[11] C. Attaianese, V. Nardi, and G. Tomasso, "A novel SVM strategy for VSI dead-time-effect reduction," *IEEE Trans. Ind. Appl.*, vol. 41, no. 6, pp. 1667–1674, Nov./Dec. 2005.

[12] A. C. Oliveira, C. B. Jacobina, and A. M. N. Lima, "Improved dead-time compensation for sinusoidal PWM inverters operating at high switching frequencies," *IEEE Trans. Ind. Electron.*, vol. 54, no. 4, pp. 2295–2304, Aug. 2007.

[13] L. Chen and F. Z. Peng, "Dead-time elimination for voltage source inverters," *IEEE Trans. Power Electron.*, vol. 23, no. 2, pp. 574–580, Mar. 2008.

[14] Y.-K. Lin and Y.-S. Lai, "Dead-time elimination of PWM-controlled inverter/converter without separate power sources for current polarity detection circuit," *IEEE Trans. Ind. Electron.*, vol. 56, no. 6, pp. 2121–2127, Jun. 2009.

[15] C. Song, N. Diao, Z. Xue, X. Sun, and J. Guan, "Tri-carrier sinusoidal pulse-width modulation without dead time effects for converters," *IET Power Electron.*, vol. 8, no. 10, pp. 1941–1951, 2015.

[16] Q. Yan et al., "A double-modulation-wave PWM with reduced dependency on current polarities for dead-time-effect elimination in three-level t-type converters," *IEEE Trans. Power Electron.*, vol. 36, no. 7, pp. 8413–8427, Jul. 2021.

[17] H.-S. Kim, H.-T. Moon, and M.-J. Youn, "On-line dead-time compensation method using disturbance observer," *IEEE Trans. Power Electron.*, vol. 18, no. 6, pp. 1336–1345, Nov. 2003.

[18] N. Urasaki, T. Senjyu, K. Uezato, and T. Funabashi, "An adaptive dead-time compensation strategy for voltage source inverter fed motor drives," *IEEE Trans. Power Electron.*, vol. 20, no. 5, pp. 1150–1160, Sep. 2005.

[19] S.-Y. Kim, W. Lee, M.-S. Rho, and S.-Y. Park, "Effective dead-time compensation using a simple vectorial disturbance estimator in PMSM drives," *IEEE Trans. Ind. Electron.*, vol. 57, no. 5, pp. 1609–1614, May 2010.

[20] A. Cichowski and J. Nieznanski, "Self-tuning dead-time compensation method for voltage-source inverters," *IEEE Power Electron. Lett.*, vol. 3, no. 2, pp. 72–75, Jun. 2005.

[21] M. A. Herran, J. R. Fischer, S. A. Gonzalez, M. G. Judewicz, and D. O. Carrica, "Adaptive dead-time compensation for grid-connected PWM inverters of single-stage PV systems," *IEEE Trans. Power Electron.*, vol. 28, no. 6, pp. 2816–2825, Jun. 2013.

[22] S. R. Bowes and B. M. Bird, "Novel approach to the analysis and synthesis of modulation processes in power convertors," *Proc. Inst. Elect. Engineers*, vol. 122, no. 5, 1975, pp. 507–513.

[23] J. Ye, S. Huang, L. Liu, L. Li, J. Xu, and A. Shen, "Accurate harmonic calculation for digital SPWM of VSI with dead-time effect," *IEEE Trans. Power Electron.*, vol. 36, no. 7, pp. 7892–7902, Jul. 2021.

[24] S. Huang, J. Xu, J. Ye, and A. Shen, "Generalized accurate harmonic calculation method based on discretized double fourier series to solve double-pulse phenomenon," *IEEE Trans. Ind. Electron.*, to be published, doi: 10.1109/TIE.2022.3194572.

[25] J. Ye, A. Shen, Z. Zhang, J. Xu, and F. Wu, "Systematic design of the hybrid damping method for three-phase inverters with high-order filters," *IEEE Trans. Power Electron.*, vol. 33, no. 6, pp. 4944–4956, Jun. 2018.

Jie Ye was born in Hubei Province, China, in 1989. He received the B.S. degree in software engineering from Xidian University, Xian, China, in 2011 and the Ph.D. degree in control science and engineering from the School of Automation, Huazhong University of Science and Technology, Wuhan, China, in 2017.

He is currently a Lecturer with the Huazhong University of Science and Technology. His research interests include signal processing, circuit theory, harmonics suppression, and reactive power compensation.

Yukai Huang was born in Henan Province, China, in 1998. He received the B.S. degree in automation in 2020 from the School of Artificial Intelligence and Automation, Huazhong University of Science and Technology, Wuhan, China, where he is currently working toward the Ph.D. degree in control science and engineering.

His research interests include power electronics, dead time effect, harmonics suppression, and modern control theory.

Songtao Huang (Graduate Student Member, IEEE) was born in Hubei Province, China, in 1994. He received the B.S. degree in automation from the School of Control Science and Engineering, Shandong University, Shandong, China, in 2017. He is currently working toward the Ph.D. degree in control science and engineering with the School of Artificial Intelligence and Automation, Huazhong University of Science and Technology, Wuhan, China.

His research interests include power electronics, dead time effect, harmonics suppression, and optimization algorithms.

Haozhe Wang (Student Member, IEEE) was born in was born in Hubei Province, China, in 1997. He received the B.S. degree in automation in 2019 from the School of Artificial Intelligence and Automation, Huazhong University of Science and Technology, Wuhan, China, where he is currently working toward the Ph.D. degree in control science and engineering.

His research interests include power electronics, harmonics suppression, circuit theory, and stability analysis.

Baojin Li was born in Anhui Province, China, in 1992. He received the B.S. degree in automation from the Department of Electronic Information and Electrical Engineering, Dalian University of Technology, Dalian, China, in 2016. He is currently working toward the Ph.D. degree in control science and engineering with the School of Artificial Intelligence and Automation, Huazhong University of Science and Technology, Wuhan, China.

His current research interests include power electronics, harmonics suppression, and circuit theory.

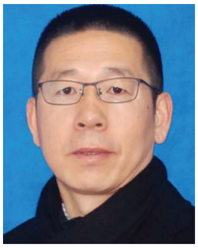

Jinbang Xu was born in Hubei, China, in 1973. He received the Ph.D. degree in control science and engineering from the Department of Control Science and Engineering, Huazhong University of Science and Technology (HUST), Wuhan, China, in 2004.

He is currently a Professional with the School of Automation, HUST. His research interests include power electronics, intelligent control, and smart grid.

Anwen Shen (Member, IEEE) received the B.S. and M.S. degrees in automation from Zhejiang University, Zhejiang, China, in 1991 and 1994, respectively, and the Ph.D. degree in automation from the Huazhong University of Science and Technology (HUST), Wuhan, China, in 1997.

In 1997, he joined the Department of Control Science and Engineering, HUST, where he is currently a Professor with the School of Automation. He is a holder of more than ten patents. His research interests include advanced motion control, power electronic applications, motor drives, electrical vehicles, and intelligent control.